Book of Tutorials and Abstracts

European Microbeam Analysis Society

EMAS 2023

17th

EUROPEAN WORKSHOP

on

MODERN DEVELOPMENTS AND APPLICATIONS IN MICROBEAM ANALYSIS

7 to 11 May 2023
at the
Jagiellonian University, Auditorium Maximum
Krakow, Poland

Under the auspices of the Rector of the
Jagiellonian University, Krakow, Poland
Organised in collaboration with the
Institute of Metallurgy and Materials Science of
the Polish Academy of Sciences, Krakow, Poland

EMAS
European Microbeam Analysis Society eV
www.microbeamanalysis.eu/

This volume is published by:
European Microbeam Analysis Society eV (EMAS)
EMAS Secretariat
c/o Eidgenössische Technische Hochschule, Institut für Geochemie und Petrologie
Clausiusstrasse 25
8092 Zürich
Switzerland

ISBN 978 90 8227 6961
NUR code: 972 – Materials Science

HYPERSPY: OPEN-SOURCE MULTI-DIMENSIONAL ANALYSIS SOFTWARE FOR ELECTRON MICROSCOPY

Håkon W. Ånes[1], P. Crout[2], N. Cautaerts[3], K.E. MacArthur[4], E. Prestat[5], J. Hjelen[1], A.T.J. van Helvoort[6] and K. Marthinsen[1]

1 Norwegian University of Science and Technology (NTNU), Department of Materials Science and Engineering
Gløshaugveien 15, 7030 Trondheim, Norway
2 University of Cambridge, Department of Material Science and Metallurgy
Cambridge, Great Britain
3 Flemish Institute for Technological Research (VITO)
Boeretang 200, 2400 Mol, Belgium
4 Oxford Instruments Nanoanalysis
Halifax Road, High Wycombe HP12 3SE, Great Britain
5 Culham Centre for Fusion Energy
Abingdon, Great Britain
6 Norwegian University of Science and Technology (NTNU), Department of Physics
7491 Trondheim, Norway
e-mail: hakon.w.anes@ntnu.no

Håkon Wiik Ånes grew up in Bergen on the west coast of Norway. He received his MSc in applied physics from the Norwegian University of Science and Technology (NTNU) in Trondheim, working with Antonius T.J. van Helvoort on photochromic thin films in the transmission electron microscope. He is currently a PhD candidate at NTNU, working with Knut Marthinsen and van Helvoort on recrystallisation in aluminium alloys using electron microscopes. He is a contributor to HYPERSPY and many related open-source projects, including KIKUCHIPY, which extends HYPERSPY's capabilities to processing, simulating and indexing electron backscatter diffraction (EBSD) patterns. He has published 8 journal papers.

1. ABSTRACT

HYPERSPY is an open-source software for interactive analysis of multi-dimensional signals acquired in either a transmission or scanning electron microscope (TEM, STEM or SEM). In this tutorial, we will describe the general structure and capabilities of HYPERSPY and some of its signal specific extensions. Application examples from the materials community will then be given, with the goal of encouraging interested readers to apply the available software capabilities on their own data.

2. INTRODUCTION

When assessing the reliability of microbeam analysis techniques, taking account of the FAIR guiding principles [1] for scientific data management and stewardship is important. The principles outline a means to improve the infrastructure and support the reuse of scholarly data by focussing on findability, accessibility, interoperability and reusability. They do not only apply to 'data' in the conventional sense, but also to algorithms, tools and workflows that lead to the data. Open-source software is instrumental for implementing these principles in the community.

HYPERSPY [2] is an open-source Python software for multi-dimensional data analysis that provides a wide range of features for electron microscopy. Building on the outstanding range of high-quality scientific libraries in the Python language ecosystem, it offers powerful tools for accessing, visualising, analysing and storing multi-dimensional datasets, both big and small. Transparent and reproducible workflows can be written with a minimal amount of code in Jupyter notebooks [3] or scripts. Many readers of common file formats for electron microscopy are available, making workflows format agnostic.

HYPERSPY itself offers functionality to analyse electron energy-loss spectra (EELS) [4], energy-dispersive X-ray spectra (EDS) from scanning electron microscopy (SEM) [5] or transmission electron microscopy (TEM) [6], and electron holography images [7]. Additionally, the software provides an easy way for other Python packages to extend its tools to analyse other multi-dimensional signals. Examples of such packages, as illustrated in Fig. 1, are PYXEM [8] for diffraction patterns from 4D scanning TEM (4D-STEM) [9], ATOMAP for atomic resolution STEM images [10], LUMISPY [11] for luminescence spectra [12], and KIKUCHIPY [13] for electron backscatter diffraction (EBSD) patterns [14]. Through a common, simple syntax, HYPERSPY and its extensions aim at lowering the entry barrier to advanced interactive data analysis to non-professional programmers, like materials scientists. These softwares are community driven, with development in large part done on a voluntary basis. Contributors come from different parts of the microscopy community, which is reflected in the range of available extensions.

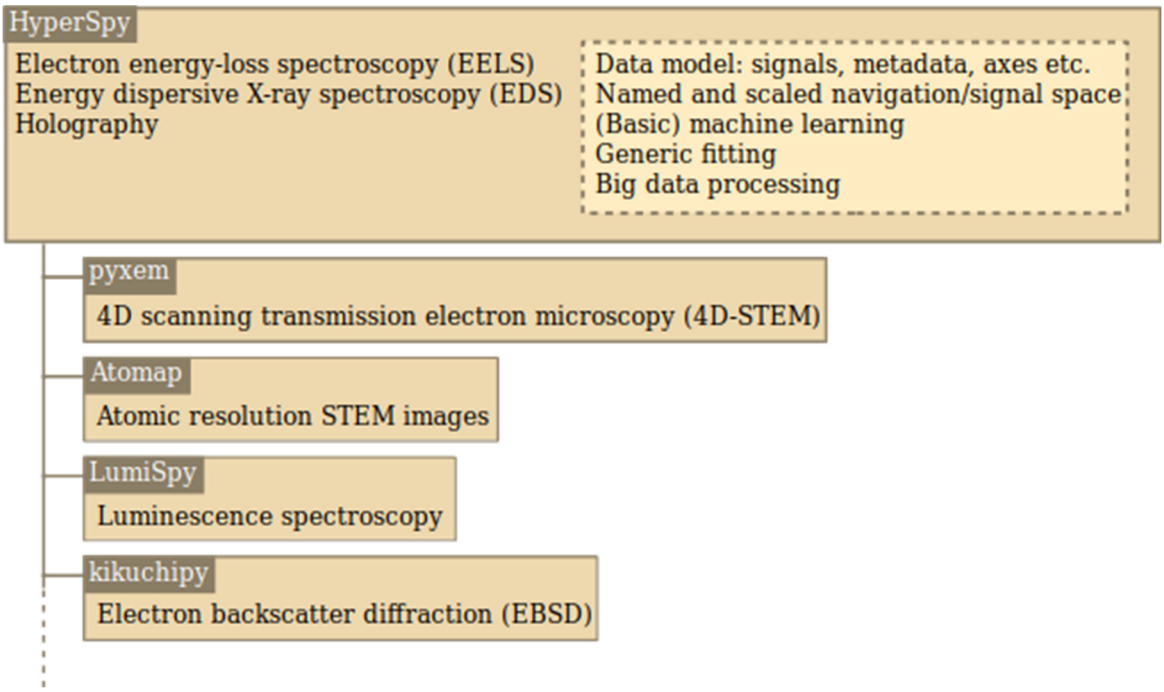

Figure 1. Application specific signals in HYPERSPY and extensions PYXEM, ATOMAP, LUMISPY and KIKUCHIPY. Note that the list is not exhaustive. Some of the core tools available to all signals are also listed in the HYPERSPY box.

An overview of the HYPERSPY package and its extensions PYXEM and KIKUCHIPY is given in the following section. The goal is to briefly touch on most of the available functionality, and rather refer to relevant literature for further details. To give an impression of what is possible with these packages, application examples for TEM-EDS, EELS, 4D-STEM and EBSD are then given.

3. *THE HYPERSPY PACKAGE AND ITS EXTENSIONS*

When a user loads data from file with HYPERSPY or any of its extensions, a 'signal' specific to the data in the file is returned, e.g., an EDS spectrum acquired in the TEM or a dataset of EBSD patterns acquired in the SEM. These signals are the main point of user interaction. In addition to the data in the file, most readers try to read as much as possible of the metadata in the file, like beam energy and sample tilt. This information is combined in signals for easy access and inspection, and metadata can be updated if necessary. By keeping track of named data axes, typically one or two navigation axes and one or two signal/detector axes, the data can be sliced, visualised or operated upon along any axis. Numerous qualitative and quantitative analysis approaches are available, like generic 1D and 2D fitting and basic machine learning, some specific to particular signals. Users can define their own function operating on a single unit of the signal (e.g. a spectrum or a pattern), and then map this function across the whole navigation

dimension. Additionally, most operations can be performed seamlessly on datasets too large to fit into available computer memory (RAM) by processing the data one chunk at a time (so-called 'lazily').

The following is an example of the Python syntax to load a line scan of EELS spectra and visualise them:

```
import hyperspy.api as hs
s = hs.load("LSMO_STO_linescan.hdf5")
s.plot()
```

Following initial visual inspection of the EELS spectrum, options are available to estimate the absolute thickness of the TEM sample from a low-loss spectrum, estimate and align the zero-loss peak for more accurate quantification, perform deconvolution to remove the effects of plural scattering, estimate the complex permittivity of the sample via Kramers-Kronig analysis and more. Absolute quantification can be done by curve fitting using a model composed of individual components including a power law for the plasmon background, a specialised component for each core-loss edge, etc. The core-loss edge components are modelled on theoretical cross-sections following Ray Egerton's hydrogenic cross-sections [4], or licensed Hartree-Slater GOS from Digital Micrograph if available. Fitting can then be done in an iterative manner along the energy-loss axis from background, background and first edge, etc., until all edges are fit simultaneously. All aspects of the fitting can be controlled, including whether fine structure should be accounted for. Importantly, an optimal fit can be found iteratively by visual feedback of intermediate results.

Turning to EDS, intensity maps from various elements in a volume of material can be obtained either by integrating peak intensities through window integration or by curve fitting, similar to the procedure for EELS but using a polynomial to model the background and Gaussians to model EDS lines. For TEM-EDS, quantification can be done using one of three approaches to convert the intensities to element composition: the original Cliff-Lorimer ratio approach using *k*-factors [15], or the comparatively new related methods of Zeta-factors [16] or partial cross-sections [17]. The factors used must be provided by the user. The two latter approaches additionally require the live time and beam current. Absorption correction for parallel-sided thin-film samples from a single detector is available for all methods, but a thickness map must be provided to make it possible for the *k*-factor method. Note that HYPERSPY currently does not provide ZAF correction [5] of the effects of atomic number (Z), absorption (A) and fluorescence (F) excitation of SEM-EDS spectra.

HYPERSPY makes it easy to apply multivariate analysis (MVA) methods to signals through seamless integration with the Python package SCIKIT-LEARN [18]. By assuming that spectra or set of diffraction patterns are described by a finite number of 'components' and noise, various algorithms can be employed to estimate these components. This can be useful for noise and

dimensionality reduction. Or, with some care and additional analysis, components can be used in quantification. This approach to quantification of EELS or EDS spectrum images (SI's) has proven particularly useful, and two examples of its use to quantify titanium and oxide phases in multilayers with EELS [19] and the chemical composition of core-shell nanoparticles with EDS [20] are revisited in sections 4.1 and 4.2, respectively.

The PYXEM package extends HYPERSPY for analysis of 4D-STEM diffraction patterns [9], with a focus on spot patterns. Functionality includes (interactive) virtual dark field imaging, differential phase contrast imaging [21], mapping of lattice strain, nano-crystal segmentation [22], mapping of short-range order in amorphous materials using (radial) pair distribution functions [23] or angular correlations [24] and phase and orientation mapping via template matching [25]. An example of orientation mapping of a nanocrystalline Cu-Ag alloy is given in section 4.3.

The KIKUCHIPY package extends HYPERSPY for analysis of EBSD patterns [14]. The package focusses on phase and orientation mapping, so-called indexing. Three modes of indexing are supported: Hough indexing [27-29], dictionary indexing [30], and orientation and/or projection centre (PC) refinement [31]. Hough indexing is enabled through interoperability with PYEBSDINDEX [32]. Dictionary indexing and refinement rely on EBSD simulations. Although KIKUCHIPY can perform both geometrical [33] and kinematical simulations, best indexing results are by far obtained using dynamical simulations, which can be obtained e.g., with EMSOFT [34]. An example of indexing Al and Si in a Sr-modified Al-10wt%Si alloy is given in section 4.4.

Documentation complete with an extensive user guide and descriptions of all classes, functions and methods in HYPERSPY is available via https://hyperspy.org/hyperspy-doc/current, and the source code [9] is hosted at https://github.com/hyperspy/hyperspy. Likewise, PYXEM's documentation and source code is available at https://pyxem.readthedocs.io and https://github.com/pyxem/pyxem, respectively, while KIKUCHIPY's documentation and source code is available at https://kikuchipy.org and https://github.com/pyxem/kikuchipy. Many operations in HYPERSPY are available in the graphical user interface (GUI), HYPERSPYUI [35], offering a simple and intuitive interface to HYPERSPY. A screenshot of HYPERSPYUI is shown in Fig. 2.

4. APPLICATION EXAMPLES

4.1. Quantitative electron energy-loss spectroscopy

Accurate quantitative mapping of the composition of micro- and nanostructures with EELS can be challenging when excitation edges overlap. The conventional approach of background correction followed by window integration of intensities struggles when edges overlap. Even physically informed curve fitting using theoretical cross-sections can run into difficulties with

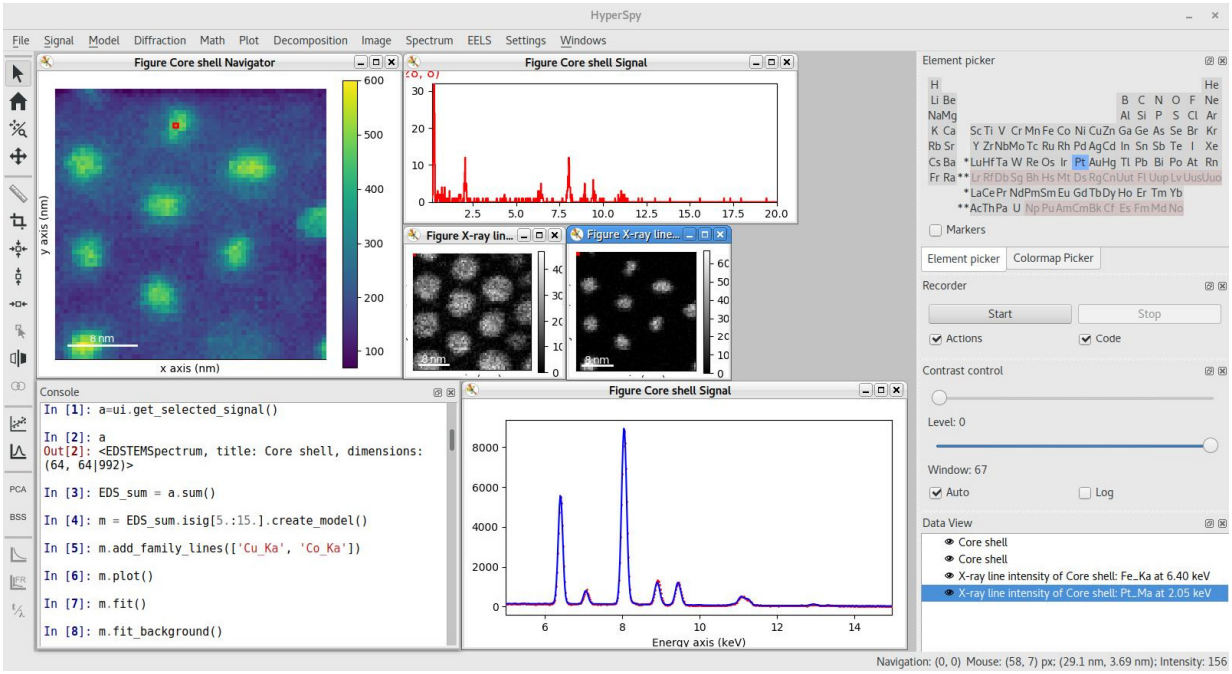

Figure 2. Screenshot of HYPERSPYUI performing quantification by curve fitting of an EDS spectrum image of FePt core-shell nanoparticles. Quantification of this dataset is given as an application example in section 4.2. Reproduced from [2].

severely overlapping edges. In an EELS SI where conventional analysis struggles, de la Peña and co-workers [19] demonstrated that MVA techniques are still able to extract quantitative maps. The material in question was a TiO_2-SnO_2 solid solution consisting of alternating Ti- and Sn-rich layers. Fig. 3 shows a high-angle annular dark field (HAADF) STEM image (acquired simultaneously with the EELS SI) as well as elemental maps for O, Sn, Ti and C generated by the integration method [4]. The Sn-map is noisier than the Ti-map due to the nominal onset of the Sn-M edge being within the fine structure of the Ti-$L_{2,3}$ edge as well as its delayed broad maximum being on top of the O-K signal.

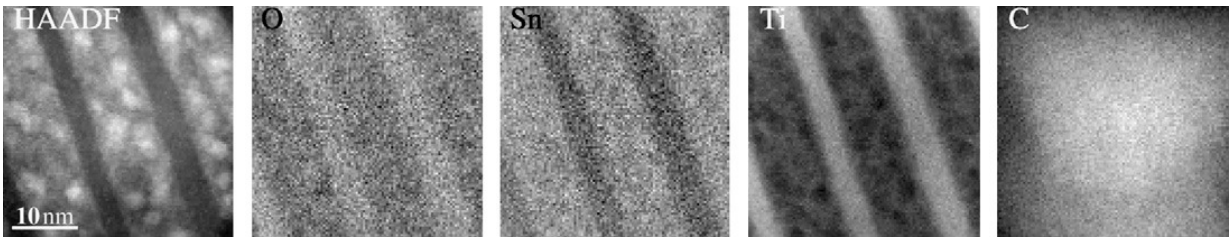

Figure 3. HAADF image and O, Sn, Ti and C elemental maps obtained by the integration method. Reproduced from [19].

Decomposing the SI with weighted principal component analysis (PCA), accounting for Poissonian noise, shows that most of the total variance of the data is retained in the first three

components. The corresponding component spectra and intensity maps are shown in the left panel in Fig. 4. The first two principal components are identified as a non-physical mixture of, at least, Ti, Sn and O, making their associated intensity maps difficult to interpret in chemical terms. The third principal component can be roughly identified as a mixture of Ti and O. By assuming that the first derivatives of the spectra corresponding to each compound present in the sample are mutually independent, independent component analysis (ICA) should be able to determine the mixing matrix and therefore retrieve the physical components from the principal components. Applying ICA to the principal components from PCA results in the independent components and their intensity maps in the right panel in Fig. 4. The first component's intensity map is very similar to the carbon map in Fig. 3. The second component is very similar to the spectrum of TiO_2 in the rutile phase. The third component is similar to the spectrum of SnO_2. Interestingly, this component does not resemble any individual spectrum in the data as it lacks signal from Ti, although Ti is always present at quite significant levels in the data.

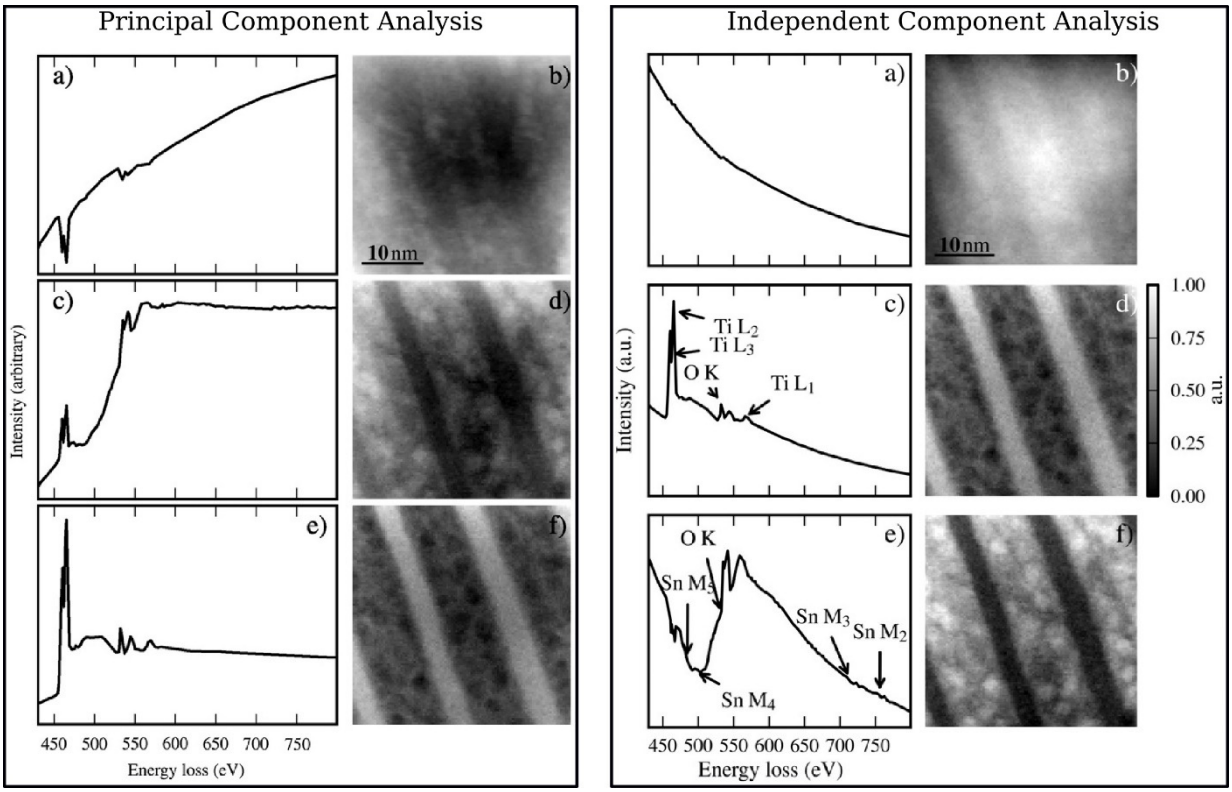

Figure 4. Left panel: The first three significant components and their corresponding intensity maps, extracted with PCA. Right panel: Independent components and their intensity maps from the components in the left panel, as determined with ICA. Adapted from [19].

The above multivariate analysis is not directly usable for quantification of elemental distributions in the sample. Using background subtraction and physically informed curve fitting of the TiO_2 independent component gives an O/Ti ratio of 1.73 +/- 0.06, but this approach does not work for

the SnO_2-component due to the overlap between O and Sn edges. By assuming that the intensity of the two oxide components at each point would be complementary in terms of composition, and neglecting other factors, de la Peña *et al.* [19] were able to normalise the independent components via two different methods: using the standard deviations in each image and fitting a parametric model to the HAADF image in Fig. 3. Both approaches produce consistent results. Finally, dividing each volume-calibrated component image by their sum should give for each point the volume fraction of the relevant substance present in the oxide material. The result is shown in Fig. 5. The average pixel values, whose only constraint is that their sum must be 1, are 0.497 for TiO_2 and 0.503 for SnO_2. This ratio is close to the nominal 50 % composition of each compound present in the mixture.

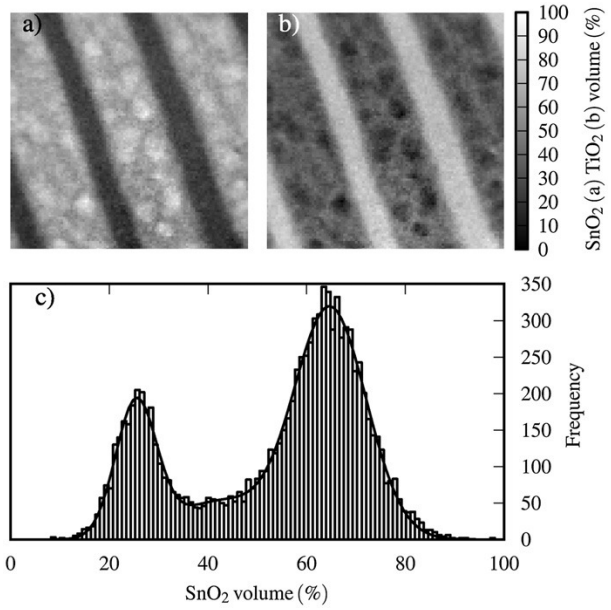

Figure 5. a) Second and b) third independent component percentage of the total thickness map, and c) histogram of the Sn thickness distribution and three Gaussians model. Reproduced from [19].

This example shows that applying the MVA techniques of weighted PCA and ICA to EELS can provide quantitative maps of various oxide proportions in mixed oxide systems for which conventional EELS analysis is unsatisfactory.

4.2. Quantitative energy-dispersive X-ray spectrometry in TEM

Heterogeneous volumes are particularly challenging to characterise with EDS in regions where there is spatial overlap of different phases within the beam path. A material system where this is an issue is core-shell nanostructures like $Co@Fe_3O_4$ and $FePt@Fe_3O_4$, which can be used as

building blocks to form nanocomposites with enhanced magnetic properties. Rossouw and co-workers [20] showed that un-mixing of the EDS spectra from these core and shell structures was possible using a similar approach as described in section 4.1.

Figure 6a shows an HAADF STEM image of FePt@Fe_3O_4 nanoparticles, acquired simultaneously with an EDS SI. Elemental maps of the various elements are shown in Figs. 6c to 6e. The image and maps show a bimetallic iron/platinum core surrounded by an iron oxide shell in most particles. From these conventional maps, one cannot tell whether the particles contain a pure platinum core surrounded by an iron oxide shell or whether iron is alloyed with platinum to form a bimetallic core. Addressing this issue, Rossouw *et al.* [20] performed weighted PCA followed by ICA of the first derivative of the PCA spectral components. The first derivative was used in order to reduce the correlation between components caused by the EDS background. Inspection of the variance ratio of the first principal components, given in Fig. 6b, suggests that there are only three phases present in the sample. The independent component intensity maps and spectra obtained from these three principal components are shown in Figs. 6f to 6i. Disregarding the small copper peaks contained in all the independent components (which originates from the support copper grid), IC#0 contains iron and platinum X-ray peaks, IC#1 iron and oxygen peaks and IC#2 a single carbon peak. These three independent components appear to belong to the three phases in the originally scanned area: core, shell and supporting film. The reliability of this result was assessed by acquiring EDS SIs of bare FePt seed particle clusters and comparing the composition in the cores obtained from curve fitting. The average composition of the bimetallic seeds was 82.0 at % Pt and 18.0 at % Fe with a standard deviation of 3.3 at %, while the composition from IC#0 was 84.9 at% Pt, which lies well within one standard deviation of the average bimetallic seed composition. This agreement suggests that this so-called blind source separation approach can be used to accurately quantify EDS spectra from regions where there is spatial overlap of different phases within the beam path. Note that the raw data and workflow necessary to produce the results in Fig. 6 are available as part of HYPERSPY's user guide.

4.3. Orientation mapping in TEM

Scanning (precession) electron diffraction [S(P)ED] relies on scanning an electron beam with a small convergence angle (on the order of 1 mrad) across an electron transparent sample whilst capturing a diffraction pattern at each scan point. A common approach for extracting phase and orientation information from these patterns is to use template matching, whereby patterns are compared to a large library of pre-computed templates of simulated patterns [26]. Recent improvements in detector technology means that such datasets become larger and the analysis pipelines more complex, making it increasingly important for the analysis to be traceable and reproducible (FAIR). For these reasons, a fast, scalable and flexible template-matching workflow was implemented in the PYXEM package by Cautaerts and co-workers [25], based on the work of Rauch and co-workers [26].

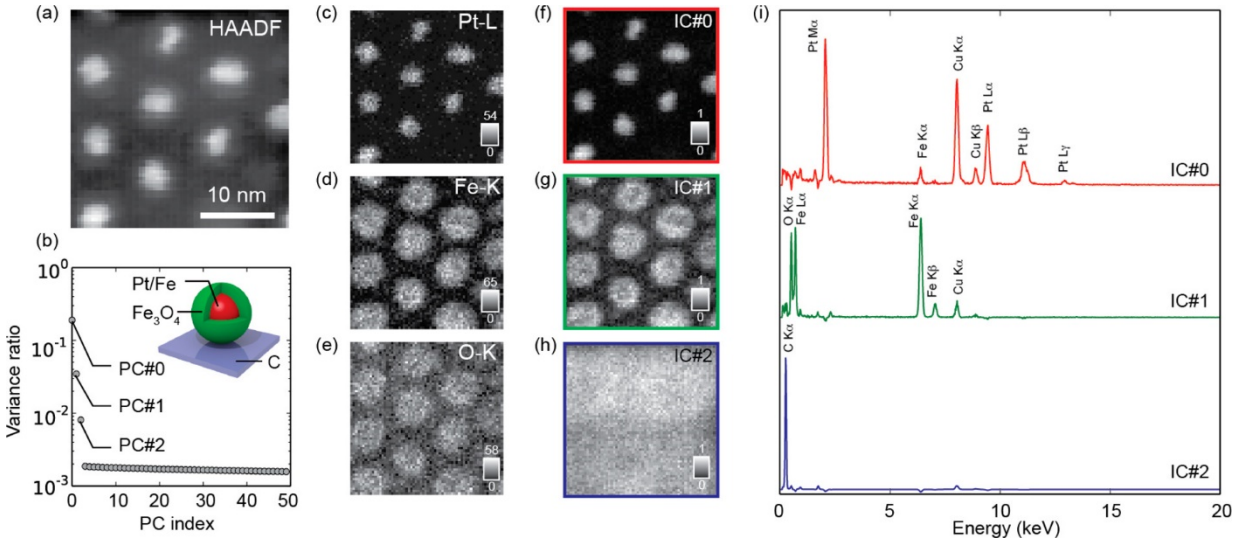

Figure 6. ICA of a cluster of bimetallic FePt nanoparticle seeds coated by Fe3O4 shells. a) HAADF STEM image. b) Data variance ratio of principal components. c-e) Elemental maps. (f-h) Intensity maps of independent components. i) Corresponding spectra of the independent components. Reproduced from [20].

In short, a template library is produced by appropriate sampling of partial orientations for a given Laue symmetry on the sphere (S2) with a set average angular resolution (typically around 1°). Following this, a calculation is performed on the relevant diffraction spots on the detector based on kinematical scattering theory. The best matching template for each pattern is then found via a correlation index score [26]. S2 sampling of orientations only give two out of three Euler angles, and the third in-plane rotation angle is found by converting both diffraction pattern and template to polar coordinates and shifting the template along the azimuthal direction. This indexing procedure is shown in Fig. 7, with the size and colour of the reflections in the template Figs. 7b and 7d serving to represent their intensity from low (blue) to high (red). The correlation index of each sampled template to the particular pattern of Fe in Figs. 7a and 7c, is shown in the inverse pole figure (IPF) in Fig. 7f. The best-fit template is taken as the solution, highlighted in Fig. 7g. If more phases are expected in a dataset, multiple libraries are compared to each pattern, and the best-fit phase and orientation is kept to produce a multi-phase map.

To assess the reliability of this implementation, results from template matching of a small region of a Cu-Ag alloy were compared with those obtained from the widely accepted commercial NanoMegas ASTAR software. The comparison is presented in Fig. 8. The IPF-Z-, -Y- and –X-maps, coloured according to crystal directions [uvw] pointing in the respective sample directions, show a high degree of similarity between the results from the two software packages. Angular deviations of the crystal directions [uvw] are shown in the third column. Differences are mostly found on grain boundaries and in regions where two or more grains overlap, and so the software each pick a different solution among these few overlapping grains. The correlation index scores in the bottom row also show a high degree of similarity. The differences in chosen orientations and scores are most likely due to different choices in image pre-processing parameters.

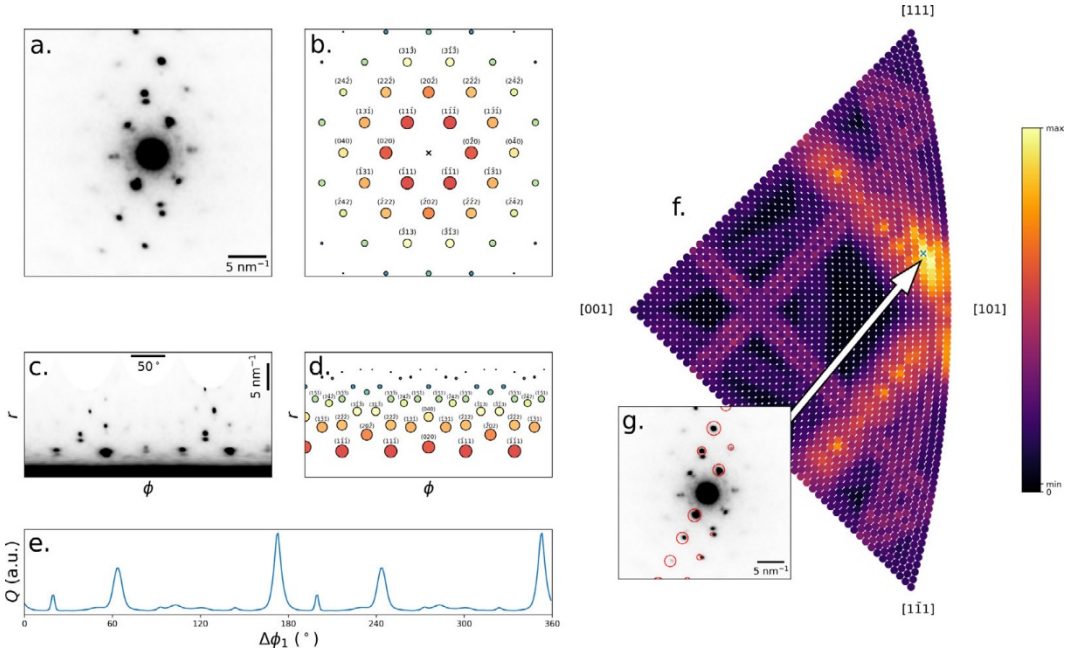

Figure 7. Illustration of the template matching indexing procedure in PYXEM. See text for details. Reproduced from [25].

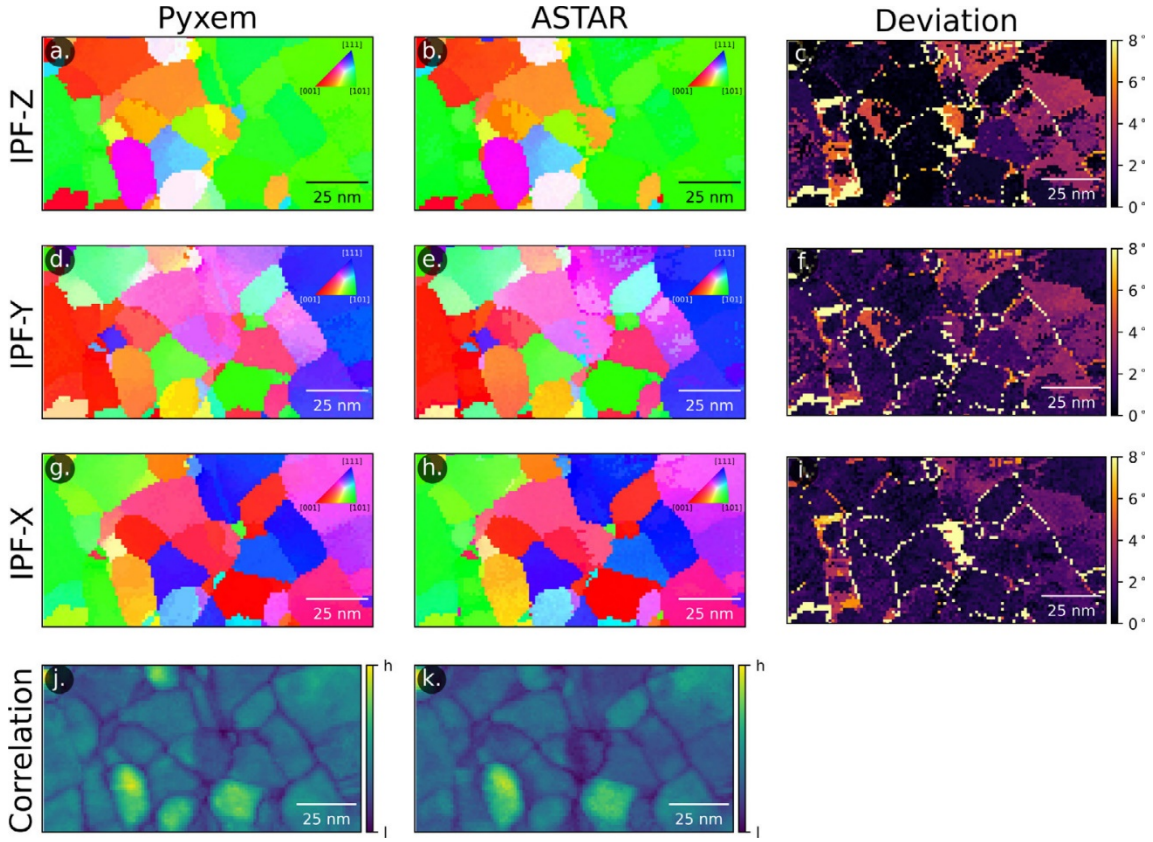

Figure 8. Comparison of indexing results from PYXEM and ASTAR. The IPF-Z map from a) PYXEM and b) ASTAR show comparable orientation solutions, reflected in the c) angle between the vectors in each pixel of a) and b). Analogous maps for d-f) IPF-Y, and g-i) IPF-X are included. j) and k) show maps comparable of correlation scores from PYXEM and ASTAR, respectively. Reproduced from [25].

In Ref. [25], Cautaerts and co-workers go on to demonstrate a two-step indexing procedure in which strong matrix reflections are masked out to enable indexing of weak precipitate reflections in an irradiated steel sample. This added flexibility, in addition to the implementation being fast by utilising the graphical processing unit, enables users to create transparent and reproducible workflows which can be run on a laptop or on a computer cluster utilising parallelisation. E.g., the raw data and workflow necessary to produce the results in the paper are available as part of the supplementary data to Ref. [25].

4.4. Phase and orientation mapping in SEM

As S(P)ED can be used for phase and orientation mapping in TEM, so can EBSD be used for the same in SEM [14]. An often-encountered problem in EBSD analysis is the challenge of differentiating between two or more phases with a similar crystal structure. Indexing methods relying solely on crystallography discard the often-crucial information in relative intensities between Kikuchi bands. An example of a material where this is the case is Al-Si alloys, where primary Al has a face-centred cubic (FCC) lattice with space group *Fm-3m* and a lattice parameter of 4.05 Å, while Si particles have a diamond cubic lattice with space group *Fd-3m* and a lattice parameter of 5.43 Å. The similarity in their crystallography is exemplified in Fig. 9a, which shows kinematical simulations of bright bands of Al in red and Si in blue in the IPF: band centres overlap, and the band widths differ only slightly. This is the reason why indexing methods, like Hough indexing, struggle with differentiating between Al and Si. Dynamical simulations, generated with EMSOFT [34], of Al and Si are shown in Figs 9b and 9c, with their difference shown in Fig. 9d. The differences are quite pronounced and reveal that Al has brighter and narrower {200} and {111} bands than Si (bright red delineated by blue in Fig. 9d), while the opposite is true for the {220} bands. These intensity differences are the main reason why indexing methods using dynamical simulations are much better at separating phases of similar crystallography but different chemistry.

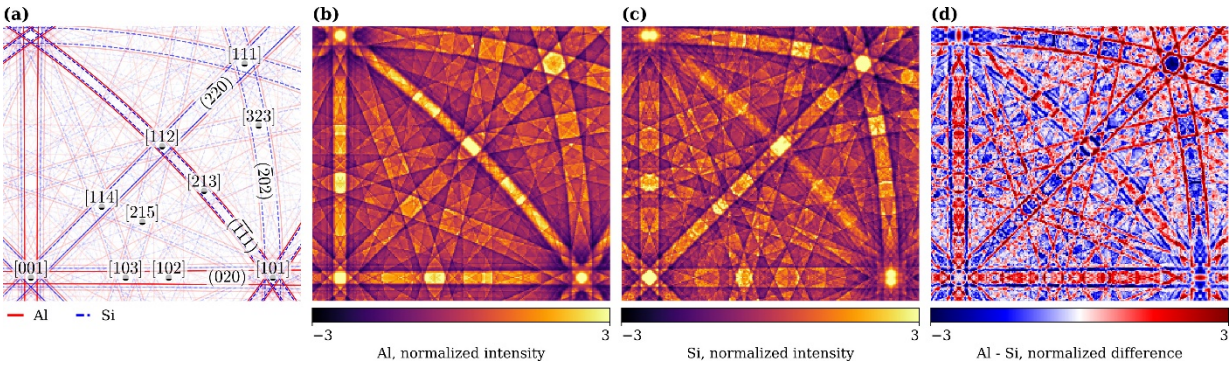

Figure 9. Differences in the diffracted signals from Al and Si, as evident from the IPF of point group *m-3m*. a) Geometrical simulation of Al (full red line) and Si (dotted blue line) with some bright low-index zone axes [uvw] and bands (hkl) highlighted. b and c) Dynamical simulations of Al and Si, with intensities normalized to a mean of 0 and a standard deviation of 1. d) Normalised difference between the dynamical simulations of Al and Si, with red (blue) corresponding to stronger Al (Si) scattering. Reproduced from [36].

To demonstrate the possibility to differentiate Al and Si based on EBSD patterns alone to showcase the indexing capabilities of the KIKUCHIPY software at the same time, indexing of a small region of Si particles in an Al eutectic in a Sr-modified Al-10wt%Si alloy is performed. Indexing is done by dictionary indexing [30] followed by orientation refinement [31]. Dictionary indexing is performed by comparing each experimental pattern to a dictionary of simulated patterns, sampled from the Rodrigues fundamental zone of proper point group 432 with an average misorientation angle of about 1.4°. Each simulated pattern in the dictionary is projected from dynamical simulations of the complete diffracting sphere (of which a part is shown in Fig. 9) onto the EBSD detector using a fixed PC. The best-fit simulation for each experimental pattern is the one with the highest normalized cross-correlation score *r*. This best-fit dictionary orientation is then refined by letting the orientation vary slightly in a controlled manner while maximising *r*. This indexing route is performed for Al and Si separately, and the final two-phase map is obtained by choosing the best-fit phase and orientation in each point. The indexing results are presented in Fig. 10.

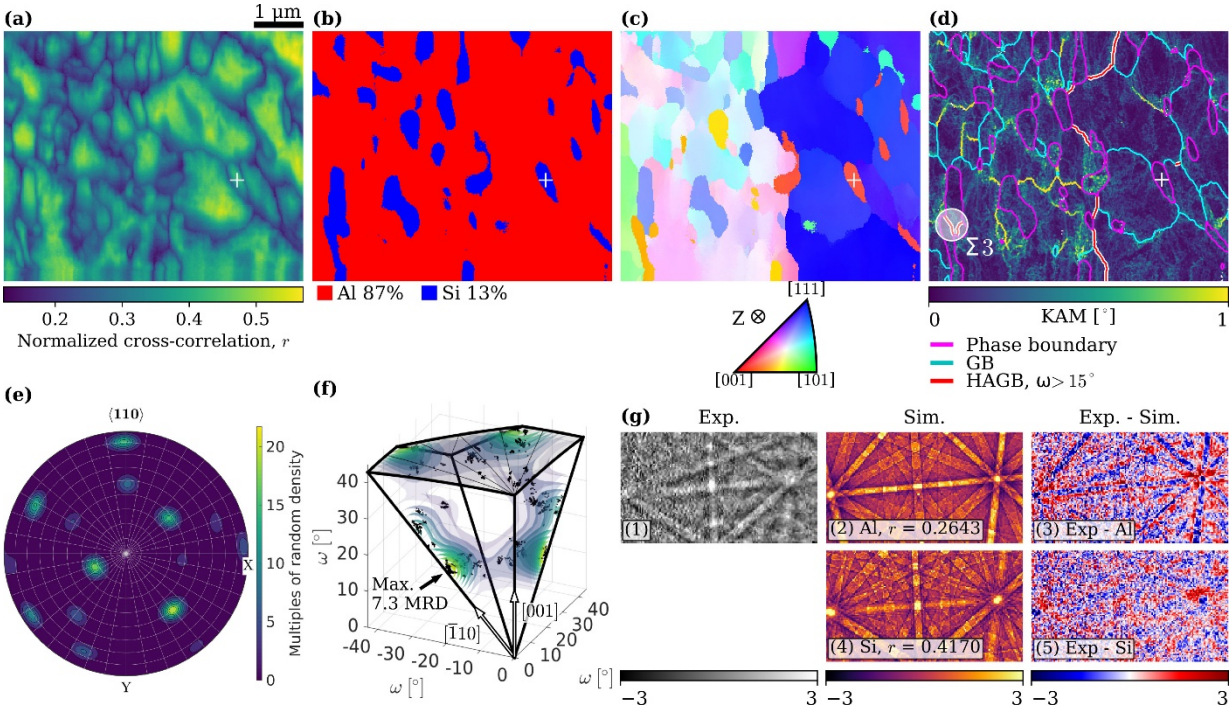

Figure 10. Indexing results from a Sr-modified Al-10wt%Si alloy. a) Normalised cross-correlation score map. b) Phase map. c) Orientation map coloured according to the inset IPF-Z map. d) Kernel average misorientation map with phase and grain boundaries highlighted according to the inset legend. e) Pole density function of <110> directions in the Si particles. f) Al-Si misorientations in Rodrigues fundamental zone of 432-432, with the maximum highlighted. g) Best-fit Al and Si simulations to an experimental pattern highlighted in (a-d). Reproduced from [36].

The score map in Fig. 10a shows that the region of interest contains many phase and (sub-)grain boundaries with lower scores, mostly due to pattern overlap. The average score is 0.3402. The microstructure of Si particles is recognisable in the phase map in Fig. 10b, which shows that 13 % of patterns match Si best. The slightly higher Si fraction than the 10 wt% in the alloy seems reasonable since Si particles are inhomogeneously distributed in between primary Al dendrites, and the solubility of each element in the other is low. The orientation map in Fig. 10c indicates that the region covers roughly two primary Al grains containing several sub-grains and that the Si particles are textured. The first observation is confirmed after reconstructing grain boundaries (with MTEX 5.8 [37]) shown in Fig. 10d, overlayed on the kernel average misorientation (KAM) map. The only high-angle grain boundaries (HAGBs), with a misorientation angle > 15°, separate the two primary Al grains and three Si particles, presumably part of the same fibre (highlighted in a circle in Fig. 10d). The HAGBs in the Si-fibre are the only Si-Si boundaries in the map, and the misorientations across these are within 3° of a 60°<111> twin misorientation (Σ3). Twin orientations are important for growth of Si-flakes and -fibres and for fibre branching [37]. Nearly all Si particles share a <110> direction as shown by the > 20 multiples of random density (MRD) maximum in the pole density function, plotted in the stereographic projection in Fig. 10e. This <110> texture was also observed by Liu and co-workers [38] in both unmodified and Sr-modified Al-12.7wt%Si alloys. No clear orientation relationship between Al and Si is observed as shown in the Rodrigues fundamental zone of the proper point groups 432-432 in Fig. 10f. The zone contains a scatter of all misorientations as well as the misorientation distribution function. The maximum in the distribution is about 7.3 MRD and corresponds to a 28°<110> misorientation, but only about 15 % of misorientations are within 5° of this maximum. The lack of an Al-Si orientation relationship in Sr-modified eutectic Al-Si alloys is a common observation (e.g., [39]). All these observations indicate that Al and Si have been indexed reliably.

Why pattern matching using dynamical simulations can distinguish between Al and Si from EBSD patterns alone is demonstrated in Fig. 10g, which shows the best-fit Al (g-2) and Si (g-4) pattern for an experimental pattern (g-1) from a medium sized Si particle highlighted by a white cross in Figs. 9a to 9d. The best-fit r for Si is about 37 % greater than for Al. The Al score is poorer mostly due to the mismatch between experimental and simulated band intensities and widths, as seen as negative values within bands in the difference pattern in (g-3). The Si bands' intensities and widths, on the other hand, correspond well to the experimental pattern, as seen from the lack of strongly correlated positive or negative values in the difference pattern in (g-5).

5. CONCLUDING REMARKS

We have in this contribution given an overview of HYPERSPY, an open-source software for multi-dimensional microscopy analysis, and its extensions for diffraction patterns from TEM (PYXEM) and SEM (KIKUCHIPY). Four application examples were presented, focussing on phase quantification using multivariate analysis techniques of EELS and EDS spectra, and phase and orientation mapping in TEM and SEM.

6. ACKNOWLEDGEMENTS

HWÅ acknowledges NTNU for financial support through NTNU Aluminium Product Innovation Centre. Nora Dahle at SINTEF Raufoss and Ingvild Runningen at NTNU are acknowledged for providing the Al-10wt%Si alloy sample and sample preparation for EBSD, respectively. The authors want to sincerely thank all the contributors to HYPERSPY, PYXEM, ATOMAP, LUMISPY and KIKUCHIPY, who have dedicated their time to building free analysis software that benefit all researchers and contribute to the foundation for open science within electron microscopy. In particular, we wish to thank the original creator of HYPERSPY, Dr F. de la Peña, and of PYXEM, Dr D. Johnstone, for their pioneering work on these softwares.

7. REFERENCES

[1] Wilkinson M D, *et al.* 2016 *Scientific Data* **3** 160018
[2] de la Peña F, *et al.* 2017 *Microsc. Microanal.* **23** (Spll 1) 214-215
[3] Kluyver T, *et al.* 2016 in: *Positioning and power in academic publishing: Players, agents and agendas*. (Loizides F and Schmidt B; Eds.) [Amsterdam, The Netherlands: IOS Press]
[4] Egerton R 2011 *Electron energy-loss spectroscopy in the electron microscope*. [New York, NY: Springer]
[5] Goldstein J I, *et al.* 2017 *Scanning electron microscopy and X-ray microanalysis*. [New York, NY: Springer]
[6] Williams D and Carter B 2009 *Transmission electron microscopy*. [New York, NY: Springer]
[7] McCartney M and Smith D 2007 *Ann. Rev. Mater. Res.* **37** 729-767
[8] Johnstone D, *et al.* 2022 pyxem Zenodo
[9] Ophus C 2019 *Microsc. Microanal.* **23** 563-582
[10] Nord M, *et al.* 2017 *Adv. Struct. Chem. Imag.* **3** 9
[11] Lähnemann J, *et al.* 2022 LumiSpy Zenodo
[12] Yacobi B G and Holt D B 2013 *Cathodoluminescence microscopy of inorganic solids*. [New York, NY: Springer]
[13] Ånes H W, *et al.* 2023 kikuchipy Zenodo
[14] Schwartz A J, *et al.* 2009 *Electron backscatter diffraction in materials science*. [New York: NY: Springer]
[15] Cliff G and Lorimer G W 1975 *J. Microscopy* **103** 203-207
[16] Watanabe M and Williams D B 2006 *J. Microscopy* **221** 89-109
[17] MacArthur K E, *et al.* 2016 *Microsc. Microanal.* **22** 71-81
[18] Pedregosa F, *et al.* 2011 *J. Mach. Learning Res.* **12** 2825-2830
[19] de la Peña F, *et al.* 2010 *Ultramicroscopy* **111** 169-176
[20] Rossouw D, *et al.* 2015 *Nano Lett.* **15** 2716-2720
[21] Nordahl G and Nord M 2023 *Microsc. Microanal.* **29** 574-579
[22] Bergh T, *et al.* 2020 *J. Microscopy* **279** 158-167

[23] Laulainen J E M, *et al.* 2022 *Nanoscale* **14** 16524-16535
[24] Huang S, *et al.* 2022 *Ultramicroscopy* **232** 113405
[25] Cautaerts N, *et al.* 2022 *Ultramicroscopy* **237** 113517
[26] Rauch E, *et al.* 2008 *Microsc. Anal.* **22** issue 116 4-7
[27] Wright S I and Adams B L 1992 *Metal. Trans. A* **23** 759-767
[28] Lassen N C K 1994 *Automated determination of crystal orientations from electron backscattering patterns*. PhD thesis. [Lyngby, Denmark: Technical University of Denmark]
[29] Morawiec A 2020 *Acta Cryst.* **76** 719-734
[30] Chen Y H, *et al.* 2015 *Microsc. Microanal.* **21** 739-752
[31] Singh S, *et al.* 2017 *J. Appl. Cryst.* **50** 1664-1676
[32] Rowenhorst D and Ånes H W 2022 https://github.com/USNavalResearchLaboratory/PyEBSDIndex
[33] Britton T B, *et al.* 2016 *Mater. Charact.* **117** 113-126
[34] Jackson M, *et al.* 2019 *Integr. Mater. Manuf. Innov.* **8** 226-242
[35] Fauske V T, *et al.* 2016 HyperSpyUI
[36] Ånes H W, *et al.* 2023 In preparation
[37] Bachmann F, *et al.* 2011 *Ultramicroscopy* **111** 1720-1733
[38] Day M and Hellawell A 1968 *Proc. R. Soc. Lond. A* **305** 473-491
[39] Liu X, *et al.* 2015 *Acta Materialia* **97** 338-347